Spin wave dispersion relations and isofrequency curve calculations using micromagnetic simulations

Matthew G. Copus¹, Alexandra R. Stuart², Robert E. Camley¹, Kristen S. Buchanan^{2,*}

¹Department of Physics, University of Colorado Colorado Springs, Colorado Springs, CO 80918

²Department of Physics, Colorado State University, Fort Collins, CO 80523

*Kristen.Buchanan@colostate.edu

Abstract

Dispersion relations and isofrequency curves are of critical importance for understanding the behavior of waves, including what frequencies can be excited, how the waves will propagate, and how waves in one system will couple to another. Here we present methods to extract the dispersion relations and isofrequency curves automatically and conveniently, each from a single micromagnetic simulation run. These methods have significant advantages in that they provide a means to obtain rapid insight into spin wave behavior in complex situations where analytic approaches are difficult or impossible. We present multiple examples to illustrate the methodology and discuss specific issues that need to be considered for the different situations.

1) Introduction

Dispersion relations provide at-a-glance insight into how any kind of wave – water waves, elastic waves, magnetic waves, etc. - will propagate in a particular situation. In magnetic materials, the waves of interest are spin waves, also known as magnons¹. Spin waves are of increasing interest as a means to transmit information and to carry out logic operations^{2–5} since spin waves span the gigahertz regime with wavelengths on the order of micrometers. Dispersion relations are also a vital tool for interpreting experiments to extract fundamental material parameters, e.g., the Dzyaloshinskii Moriya interactions (DMI) ^{6,7}, to understand the spin Seebeck effect⁸, to understand scattering processes that contribute to damping^{9,10}, and to predict and interpret nonlinear processes^{11,12}.

Many of the problems of interest at present, especially for magnonics applications, involve magnetic microstrips or nanostrips, but analytic theoretical models only exist for a narrow subset of the geometries of interest. Theoretical methods have been developed to calculate the spin wave dispersion relations in magnetic thin films for a variety of field directions using exact methods^{13,14} and an approximate matrix method¹⁵, both of which must be evaluated numerically. Theories have also been developed for multilayered thin films that are appropriate for calculating the dispersion relations for ferromagnetically coupled multilayers, exchange spring magnets, and RKKY-coupled thin films of interest for giant magnetoresistance and magnetic tunnel junctions ^{14,16–20}.

The dispersion relations for long magnetic wires are more complex as compared to those of an extended thin film because the spin waves are quantized across the width of the microstrip but quasi-continuous along the length. One common approach²¹ that works well for the surface wave or Damon Esbach (DE) geometry, where the magnetic field is in-plane and perpendicular to the length of the microstrip, is to use the dispersion relations for a continuous thin film¹⁵ and assume that the spin waves across the finite width of the strip should have quantized wavevectors $k_p = p\pi/w_{eff}^{22}$. Here, w_{eff} an effective width that is introduced to adjust for the effects of the nonuniform demagnetization field across the microstrip width and is typically slightly larger than the actual width of the microstrip, defined as $w_{eff} = w[g/(g-2)]$, where $g(\beta) = 2\pi/\beta[1+2\ln(1/\beta)]$ and $\beta = L/w$. For the DE geometry, there is also a sizeable static demagnetization field H_{demag} inside the microstrip that must be accounted for, hence the thin film dispersion relations should be calculated for a reduced effective static field of $H_{eff} = H - H_{demag}$, where H is the applied static field. More exact solutions have also been derived but only for the high symmetry field directions^{23,24}.

While some standard cases can be calculated analytically, this is not easy for many geometries, including microstrips, or for systems with complicated interactions, for example, multilayers with DMI and perpendicular anisotropy, or for external magnetic fields that are at an angle other than parallel or perpendicular to the surface or edge of a structure. As we will show, the method used to excite the spin waves can also play a role that is not captured by analytic calculations.

Micromagnetic simulations such as OOMMF²⁵ and mumax^{3 26} are routinely used to gain insight into the formation of spin textures, to calculate the dynamic response of patterned structures, and to investigate the response of a sample to driving stimuli including spin transfer torque and magneto-elastic perturbations. These simulations are typically used to investigate very specific problems and they do not immediately yield the rapid insight into dynamics that are offered by dispersion relations. Here we present and explore two simple methods that can be used to obtain broad insight into spin dynamics using micromagnetic simulations by directly calculating dispersion relations and isofrequency curves, each with a single dynamic run of the micromagnetic solver. Dispersion relations are, of course, fundamental tools for understanding and characterizing wave excitations. Isofrequency curves are equally important as they may be used to indicate the direction and magnitude of power flow and caustics from a localized source^{27–31}.

Spin wave dispersion methods

2) Sinc pulse method

The first method we will demonstrate involves the use of micromagnetic simulations to calculate dispersion relations. Micromagnetic simulations were conducted using mumax³ ²⁶ for two test cases: a Permalloy microstrip where the angles of the antenna and magnetic field are varied, and a Pt/Co/Gd trilayer magnetic microstrip. These cases, dubbed case 1a and 1b, respectively, illustrate how this method can be used to calculate dispersion relations for non-standard field

angles not covered by existing analytical theories, and for complex cases that involve interlayer exchange^{16,17} and DMI^{32,33}, effects that have been incorporated separately into spin wave dispersion theories but not yet combined. These cases also highlight that it is possible to treat inplane and out-of-plane magnetization tilts easily, whereas these add considerable complexity to analytical and semi-analytical approaches.

The geometries considered for these simulations, long magnetic micro- or nano-strips of width w and length $l\gg w$ made up of one or more magnetic layers, are illustrated in Figs. 1(a) and (b). The thicknesses of the ferromagnetic thin film layers $t_{FM1},\,t_{FM2},\,...$ are small compared to l and w. The spin wave dispersion relations are obtained by first allowing the spin state to relax to equilibrium in the presence of a static magnetic field H. In the examples considered here H is applied in-plane at an angle φ with respect to the microstrip long axis, also the x direction, but this method will work for any static field orientation. Next, a broadband excitation field is applied to a narrow region of width $w_{antenna}$ that spans the width of the magnetic nanowire to approximate the effect of a microstrip antenna. Here a broadband sinc pulse was used

$$H_{dyn} = \frac{h_0 \sin(2\pi f_c(t-t_0))}{2\pi f_c(t-t_0)},$$

applied in-plane and parallel to the antenna width, where h_0 is the pulse amplitude, and t and t_0 are time and central time of the pulse, respectively. A microstrip antenna will also generate out-of-plane fields and, while this can be included, the susceptibility of a magnetic thin film is usually an order of magnitude lower for the out-of-plane response, so for simplicity we use only the in-plane component. The bandwidth of the excitation pulse, with central frequency f_c , should be broad enough to encompass the frequency range of interest, and the width of the antenna region w_{ant} must be narrow enough to obtain a broad range of excited k, where k is the wavevector along the length of the microstrip, i.e., $w_{antenna} < \pi/k_{max}$, where k_{max} is the maximum desired wavevector.

The pulse amplitude h_0 should be large enough to produce oscillations that are above the numerical noise level outside of the antenna region but low enough that the magnetic response is still linear. Typically, a h_0 that leads to oscillations with a few percent deviation from equilibrium near the antenna region will work well, and linear behavior is confirmed by running test simulations with several h_0 values to ensure that the shapes of the calculated dispersion relations are unaffected by h_0 .

The simulations are run in the time-domain and the magnetization along the center line of the magnetic structure is saved out at roughly equal time intervals of $dt^{\sim}10$ ps or less until the response damps out, where dt must be chosen such that the Nyquist frequency $f_{Ny}=1/2dt$ is higher than the maximum frequency of interest. The dispersion relations are obtained by first interpolating the normalized z-component of the magnetization m_z vs. x and t onto a fixed time base and then taking a two-dimensional Fourier transform, over time and space. A proposed standard problem that uses OOMMF and Nmag uses a similar approach to calculate dispersion

relations for high symmetry directions, described in Ref. [34], and here we show examples of how this approach is more broadly useful for more complex situations.

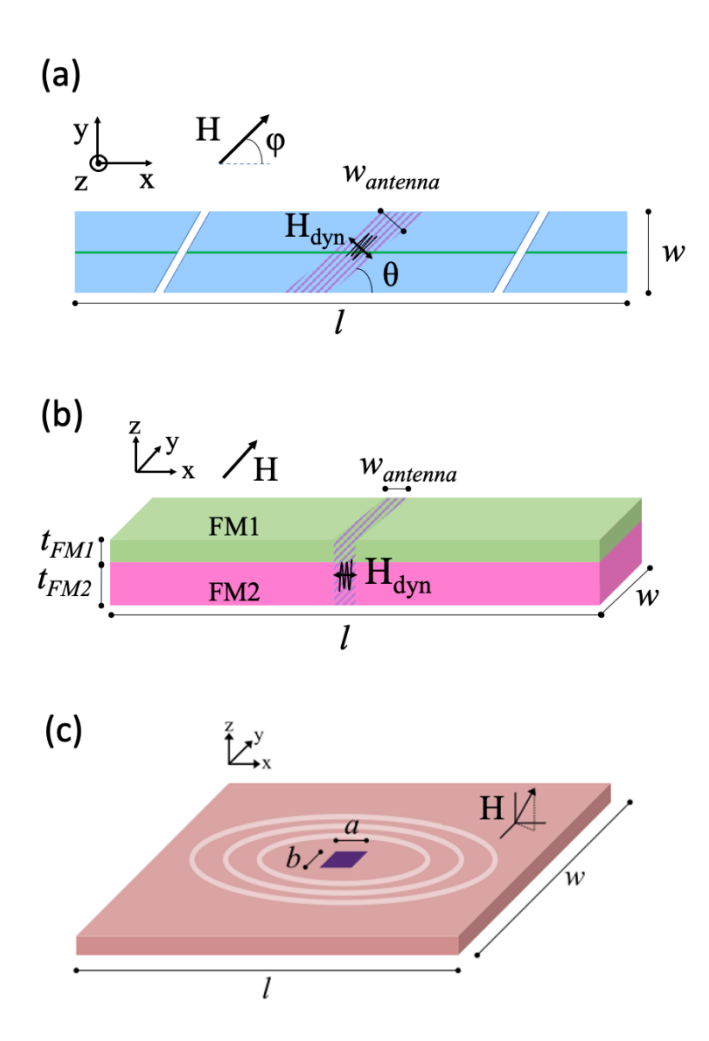


Figure 1: Geometry for the spin wave dispersion and isofrequency curve calculations. a) Top view and b) 3D view of the geometry used for spin wave dispersion calculations. The magnetic strip is made up of one or more layers of thickness t_{FM1} , t_{FM2} , etc. and has dimensions of length l along x by width w along y, with $l\gg w$. A uniform, in-plane static field H is applied to the entire strip at an angle of φ from the x-axis. A dynamic field H_{dyn} is applied within the antenna region of width $w_{antenna}$, shown by the cross-hatched area. The antenna is oriented at an angle θ with respect to x, and H_{dyn} is applied perpendicular to the antenna width. The green line in a) shows the midpoint of the microstrip in the y direction. The magnetization is saved along this line as a function of time. The slanted cuts in a) are used to illustrate that $l\gg w$. c) Diagram of the geometry used for isofrequency calculations, where a localized source is pulsed at a specific frequency. The external field can be applied at any angle. The light-colored rings indicate the anisotropic propagation of the wavefronts from the source.

The first case considered, case 1a, involves a long, straight $t_{FM1}=40$ -nm thick and w=1- μ m wide Permalloy microstrip with $\mu_o H = 0.12$ T applied in-plane at angles φ of 90°, 45°, and 60°. Spin wave dispersion relations were calculated using micromagnetic simulations for antenna orientations of $\theta = 90^{\circ}$ and $\theta = \varphi$ for each φ , as defined in Fig. 1(a). Material parameters appropriate for Permalloy were used: saturation magnetization $M_s = 8 \times 10^5$ A/m, exchange $A_{ex}=1.3\times10^{-11}$ J/m, $\gamma=1.76\times10^{11}\frac{rad}{T_{s}}$, a damping parameter of $\alpha=0.01$, and anisotropy was neglected. The dynamic magnetic field H_{dyn} was applied in-plane and perpendicular to the antenna axis within a $w_{antenna} = 100$ -nm wide region, centered with respect to the Permalloy microstrip length, with pulse parameters of f_c = 20 GHz, t_0 = 50 ps, and $\mu_o h_0$ = 1 mT. The Permalloy $l=41 \, \mu m$ microstrip length, is than w, and long enough to avoid reflections.

The cell sizes used in the dispersion and isofrequency calculations are typically of order x - 10 nm, y - 10 nm, z - t_{FM1} , where t_{FM1} is typically tens of nanometers or less. For case 1a we use cells of x - 20 nm, y - 15.6 nm, z - 40 nm, which we will indicate by 20 × 15.6 × 40 nm³. Similarly, the number of cells, for example, is indicated by 2048 x 64 x 1, meaning that there are 2048 cells in the x direction, 64 in the y direction, and 1 in the z direction. Smaller cells are needed to accurately capture domain walls where the cell size must be on the order of the exchange length of the material or smaller, but for spin wave dispersion relations the relevant length scale is the smallest spin wave wavelength of interest, consequently larger cells can often be used. Selected simulations repeated with half-sized cells yield the same results, indicating that the cells are sufficiently small.

The results for the Permalloy microstrip are shown in Fig. 2. Fig. 2(a) and (b) show the results for $\theta = \varphi = 90^{\circ}$, so H is along the microstrip width, which is the DE or surface wave geometry that is often used in experiments. The microstrip is magnetized mainly along γ , with a slight tilt along x at the top and bottom edges, a configuration known as the flower state. The magnetization m_z vs. x and t (Fig. 2(a)) shows a broadband response in the time-domain that is concentrated at the antenna for small times and spreads out in x and decreases in amplitude as t increases. The signal damps out before reaching the ends of the microstrip and no reflections are observed. The twodimensional Fourier transform of Fig. 2(a) yields the corresponding dispersion relation, shown in Fig. 2(b). The spin wave dispersion relations show the available states at a given frequency as well as the relative excitation amplitudes of the allowed modes, and the group velocity can be obtained from the slope. In Fig. 2(b) the strongest response is a quasi-continuous bright band that increases in frequency f with increasing k, where k is the wavenumber along the microstrip length. This band corresponds to the lowest-order width-quantized mode that has a single antinode at the microstrip center (along the width). For example, the strongest excitation at 12 GHz will be a traveling spin wave with lower amplitude at the edges $(y = \pm w/2)$ and the strongest amplitude at the center (y=0), a k of 6 μm^{-1} , and the group velocity $v_a=d\omega/dk$ with $\omega=2\pi f$ is approximately 2800 m/s and has the same sign as the phase velocity. Weaker dispersion relations are found at slightly lower frequencies in Fig. 2(b) as compared to the strongest mode, and these are higher-order width-quantized modes (modes with p=1,3,5..., i.e., modes with an odd number of antinodes because H_{dyn} is uniform along y). Note that excitation fields that are non-uniform across the width can be applied to excite modes with even p. Dispersion relations were also calculated analytically for the Permalloy microstrips with $\theta=\phi=90^\circ$ (Fig. 2b) using $w_{eff}=w$ and a static demagnetization field of 0.026 T, obtained from the micromagnetic simulations. The analytical calculations agree well with the dispersion relations obtained from the mumax³ simulations for p=1 and 3, and some minor deviations are present for p=5.

Analytical theories exist for the geometry considered in Figs. 2(a) and (b). These theories assume quantization of the wavevectors along w, as described in the introduction. The analytical theories have only been developed, however, for microstrips for high symmetry field directions, the DE geometry $\varphi = 90^{\circ}$ and the backward volume configuration where H is along the microstrip ($\varphi =$ 0°)^{23,24}. Several scenarios for the Permalloy microstrips that cannot be calculated using existing analytical theories are shown in Figs. 2(c-f) with $\varphi = 45^{\circ}$ and 60° with $\theta = 90^{\circ}$ where the antenna length is perpendicular to the wire and $\theta = \varphi$, i.e., where the antenna length is parallel to H. The relaxed magnetizations are in-plane and mostly uniform with magnetization angles of θ_M of 34° and 47° with respect to the x direction, respectively, for $\varphi=45^\circ$ and 60°, in both cases tilted slightly towards the long axis of the microstrip due to the shape anisotropy. Unlike the quasi-continuous mode shown in Fig. 2(b) for the DE case, the curves in Figs. 2(c-f) are made up of disconnected segments that are of similar intensity, which suggests that the wavevector quantization effects are more complex than the simple condition of width quantization ($k_p =$ $p\pi/w_{eff}$) that applies for the high symmetry directions. Notably the slopes of the individual segment are negative (positive) for positive (negative) k, so the phase and group velocities have opposite signs, which is expected for backward-volume-type waves that occur for $\varphi=0^\circ$.

The results in Fig. 2 also highlight the importance of the antenna angle θ since the accessible dispersion relations for the same φ differ significantly depending on the choice of θ . This can have important implications in terms of the number of overlapping modes available. For example, with $\varphi=45^\circ$ and $\theta=90^\circ$, a driving frequency of 12 GHz is expected to excite three modes with distinct k values based on Fig. 2(c), whereas if the antenna is tilted such that $\theta=45^\circ$, a single k would be expected at f=12 GHz (Fig. 2(d)). The effect of the antenna angle is more dramatic than the effect of the static field angle in Figs. 2(c-f). Fig. 2f shows that the combination $\varphi=\theta=60^\circ$ leads to a more complex multi-mode situation with many discrete sections that occur due to width quantization combined with the phase delays associated with the antenna angle. These results show that both φ and θ have important effects on the spin waves that can be excited in a magnetic microstrip using a strip antenna. This example also highlights how simulations can provide rapid insight (the approximate run time for the simulations in each panel of Fig. 2 is ~1 minute) for situations that are not covered by existing

analytical theories and that are relevant to magnonics, including wavevector up-conversion strategies³⁵.

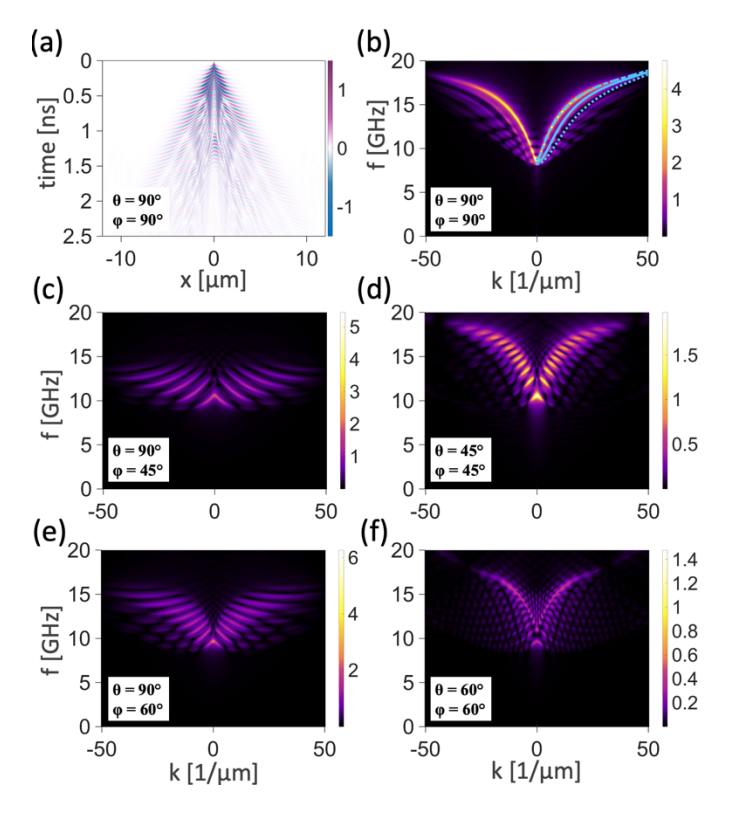


Figure 2: Dispersion relations for a 40-nm thick Permalloy microstrip with w=1 µm for selected antenna and static field orientations, θ and φ , respectively, as defined in Fig. 1a with $\mu_o H=0.12$ T. (a) Magnetization component, m_z , vs. t and x for $\theta=\varphi=90^\circ$, the DE geometry, and (b) shows the dispersion relation obtained from (a). (c) and (d) show dispersion relations for $\varphi=45^\circ$ with $\theta=90^\circ$ and 45° , respectively, and (e) and (f) show dispersion relations for $\varphi=60^\circ$ for both antenna orientations. Analytical calculations of the dispersion relations are shown in (b) for p=1,3, and 5 as blue dash-dot, solid, and dotted lines, respectively.

The second case, case 1b, involves a Co/Gd bilayer magnetic thin film with perpendicular magnetic anisotropy and interfacial DMI assigned the Co layer. The parameters used here are chosen to match those of multilayer [Co/Gd/Pt]₁₀ films that were recently shown to support antiferromagnetic skyrmions at room temperature³⁶. The Co and Gd layers were assigned $M_s = 1.196 \times 10^6$ A/m and 0.325×10^6 A/m, respectively, values appropriate for a temperature of 160 K, $A_{ex} = 20$ pJ/m and 5 pJ/m, respectively, the interlayer exchange coupling was set to J = -0.15 mJ/m², and a damping parameter of $\alpha = 0.01$ was used. An interfacial DMI of D = 2.5 mJ/m² and a perpendicular anisotropy of $K_u = 1.6 \times 10^6$ J/m³ were applied to the Co layer to account for the effects of the Co/Pt interface. The simulations were done using $t_{FM1} = 0.5$ nm for the Co layer, $t_{FM2} = 1$ nm for the Gd, with w = 256 nm. The spin waves were excited by an antenna with $w_{antenna} = 4$ nm and $h_0 = 40$ mT in the DE geometry, the same configuration

used in Fig. 2(a,b) with $\varphi=\theta=90^\circ$. The Co/Gd simulations were done with $2\times2\times0.5~\text{nm}^3$ cells and $l=2~\mu\text{m}$ and repeated with $5\times5\times0.5~\text{nm}^3$ cells and $l=10.24~\mu\text{m}$, using $1024\times128\times3$ cells in the first case and $2048\times128\times3$ cells in the second case. Both sets of simulations yielded similar results, and in both cases l was sufficiently long to avoid reflections. The simulations were repeated with D = 0 mJ/m² in order to identify features specific to the DMI.

The dispersion relations for the Co/Gd microstrip are shown in Fig. 3 for two static field values, a low field of $\mu_o H=0.5$ T and a high field of $\mu_o H=2.0$ T. The low-field equilibrium state is still partially out-of-plane, whereas the high field is sufficient to achieve a fully in-plane relaxed state. Defining the out-of-plane angle of the magnetization (measured with respect to +z) as β , the low field relaxed state involves substantial out-of-plane magnetization tilts of $\beta_{Co}=13^\circ$ (tilted towards +z) and $\beta_{Gd}=121^\circ$ (tilted towards -z) for the Co and Gd layers, respectively. The inplane tilt angle for both layers is $\theta_M=90^\circ$ (in the +y direction). The two layers are tilted in opposite directions due to the antiferromagnetic interlayer exchange, and the Gd is more inplane than the Co because perpendicular anisotropy is assigned to the Co layer. At the higher field, H is sufficiently strong that both layers are fully in-plane magnetized along H ($\theta_M=90^\circ$). As shown in Fig. 3, two distinct and continuous dispersion relations are obtained for both H values. The intensities of the two modes differ slightly depending on whether the dispersion relations are calculated using the dynamic magnetization from the Co or Gd layers, but the frequency/wavevector relationships are the same.

Focusing on Figs. 3(a) and 3(b), we examine the two mode branches in more detail. The relative phases of the dynamics in the two magnetic layers were determined by examining the magnetization vs. time while driving at fixed frequencies corresponding to $k=100~1/\mu m$ for the low (f = 25 GHz) and high (f = 50 GHz) frequency branches. In Fig. 3(a), which corresponds to the low field, the low frequency branch corresponds to out-of-phase motion of the Co and Gd, whereas the Co and Gd layers oscillate in-phase for the high frequency branch. In both cases the dispersion relations are the lowest-order width quantized modes. The low frequency branch in Fig. 3(a), mode 1, is symmetric about k=0, which is also the case for the dispersion relations shown in Fig. 2, whereas the high frequency branch, mode 2, is not symmetric about k=0. GHzscale frequency difference Δf between the spin waves at +k and -k for $|k| \leq 25 \text{ 1/}\mu\text{m}$ are observed (Fig. 3(e)), and Δf increases linearly with increasing |k|, which is expected for DE-type spin waves in magnetic thin films with interfacial DMI^{32,33}. In the high field case where both layers are fully magnetized in-plane (Fig. 3(b)), the low frequency branch (mode 1) shows a large Δf of ~5 GHz for k = 25 $1/\mu$ m and a smaller GHz-scale shift for the high frequency branch (mode 2). The observed asymmetries in the dispersion relations Figs. 3(a,e) and (b,f) become negligible when D = 0 as shown in Figs. 3(e) and (f), hence the frequency shifts are due to the DMI. The DMI value cannot, however, be extracted from the slope of the Δf vs. k curves using the simple singlelayer analysis approach^{32,33}. The results shown in Fig. 3 highlight an as-of-yet unexplored peculiarity of the effect of DMI in an exchange coupled bilayer system, where both modes in the DE configuration are affected by the DMI provided the films are sufficiently in-plane magnetized. Furthermore, these calculations show that there is strong potential for quantitatively measuring the DMI in bilayer systems and highlight the importance of field dependent measurements for extracting DMI in experiments in more complex thin film stacks.

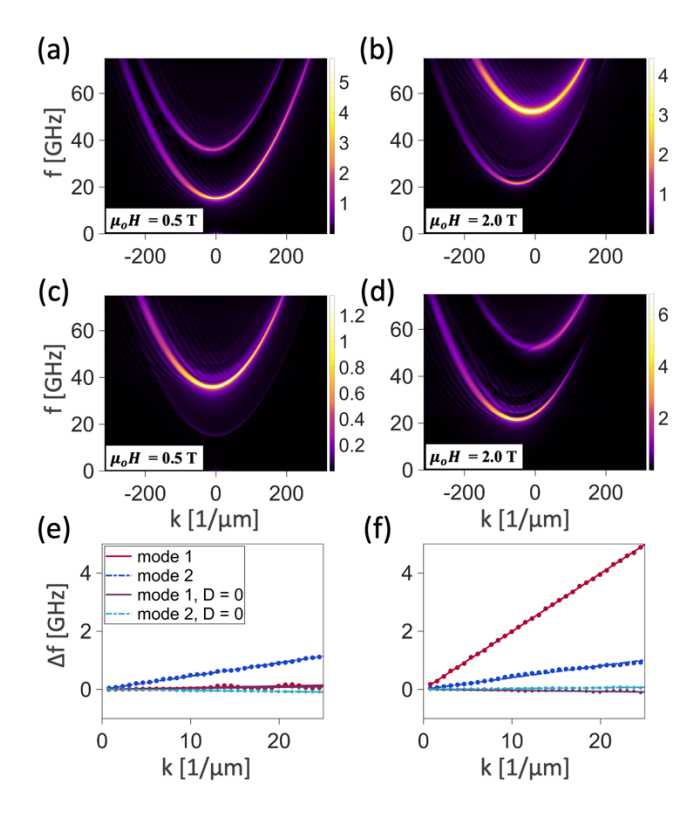


Figure 3: Dispersion relations for a CoGd bilayer microstrip with w=256 nm and D = 2.5 mJ/m² assigned to the Co layer. The thicknesses of the Co and Gd are $t_{FM1}=0.5$ nm and $t_{FM2}=1$ nm, respectively. The dispersion relations are shown in (a, c) for $\mu_oH=0.5$ T and in (b, d) for $\mu_oH=2.0$ T with $\varphi=\theta=90^\circ$. The dispersion relations calculated for the Gd and Co layers are shown in (a, b) and (c, d), respectively. The frequency differences Δf between the spin waves at +k and -k obtained from (a) and (b) are shown in (e) and (f), respectively, along with the corresponding results with no DMI (D = 0). In (e) and (f), modes 1 and 2 are the low and high frequency branches, respectively.

3) Isofrequency Curves

Isofrequency curves and propagation in arbitrary directions

The previous section developed a method to produce dispersion curves for propagation in a particular direction (along a magnetic microstrip). In contrast, here we explore a method that produces information about the dispersion curves in all directions simultaneously. In its most immediate application, this method produces a set of isofrequency curves in k space. These curves, also known as slowness surfaces in phonon problems, provide information on how a wave will spread. In particular, the density of isofrequency curves gives immediate information on group velocity $(d\omega/dk)$ in every direction. In addition, normals to the isofrequency curves indicate the direction of power flow. Finally, regions of the isofrequency curves where the curvature is zero identify the directions of caustic beams originating from point sources.^{28–31}

The identification of the connection between isofrequency curves and power flow in spin waves has become quite common with the development of microfocus Brillouin Light Scattering³⁷. The systems studied have varied from standard thin film geometries^{27,38}, thin ferromagnetic films with interfacial DMI³⁹, lens design for spin wave computing,⁴⁰ to the influence of dipole-dipole interactions in synthetic antiferromagnets.⁴¹

Our geometry consists of an extended thin film of thickness t_{FM1} as illustrated in Fig. 1(c). The z direction is oriented out of the plane of the sample and an external static field H is applied in the sample plane. The material parameters appropriate for Permalloy were used in the calculations that follow, i.e., $M_{sat}=8\times10^5$ A/m, $K_u=0$, and $A_{ex}=1.3\times10^{-11}$ J/m and $\gamma=1.76\times10^{11}\frac{rad}{T\,s}$. Unless otherwise noted, the cell size and number of cells used were 5 x 5 x 30 nm³ and 512 x 512 x 1, respectively.

In the simplest version of this method, one drives the system with an oscillating magnetic field at one or more fixed frequencies, again in a small region (one or a few cells, darker region in Fig. 1(c)), allowing a large range in wavevector space to be examined. This will produce waves in all directions with wavevectors consistent with the driving frequencies and the dispersion relations. To identify the wavevectors, we let the system evolve over time and collect the data on the transverse components of the dynamic magnetization in each cell at a particular time. We then do a two-dimensional spatial Fourier transform of $m_{\rm Z}(x,y)$, which produces iso-frequency curves in k space.

It is helpful to identify the range of wavevectors that are produced by such an excitation. The size of the sample and the size of the driven region limits the range of accessible wavevectors. If one uses a single cell, with a side dimension of a, the largest wavevector is given by

$$k_{max} = \frac{2\pi}{2a} = \frac{\pi}{a}$$

As an example, if a = 5 nm, a common value in many micromagnetics projects, then

$$k_{max} \approx 628/\mu m$$
.

This is a large value compared to those found in most spin wave dispersion curves measured with BLS or other methods. Thus, in many cases it is convenient and appropriate to use larger cell sizes, on the order of 20 - 30 nm. This allows larger systems to be more easily calculated and results in better resolution for the k values in the isofrequency curves. Some problems do emerge with larger cell sizes; this will be discussed in more detail below.

We illustrate the method with a simple example. We use the following parameters in our micromagnetic simulation for a Permalloy element which is $t_{FM1}=30$ nm thick and 5120 nm x 5120 nm wide. The parameters for the calculation are: Cell size 5 x 5 x 30 nm³; number of cells

1024 x 1024 x 1; $\mu_o H = 0.1$ T along the x axis ($\phi = 0$); Gilbert damping constant $\alpha = 0.0001$; and the oscillating field frequencies are 9, 13, 17, 21, 25, and 29 GHz. The system is driven by an oscillating field at an amplitude of 20 Oe at each frequency and in a 10 x 10 nm² central region.

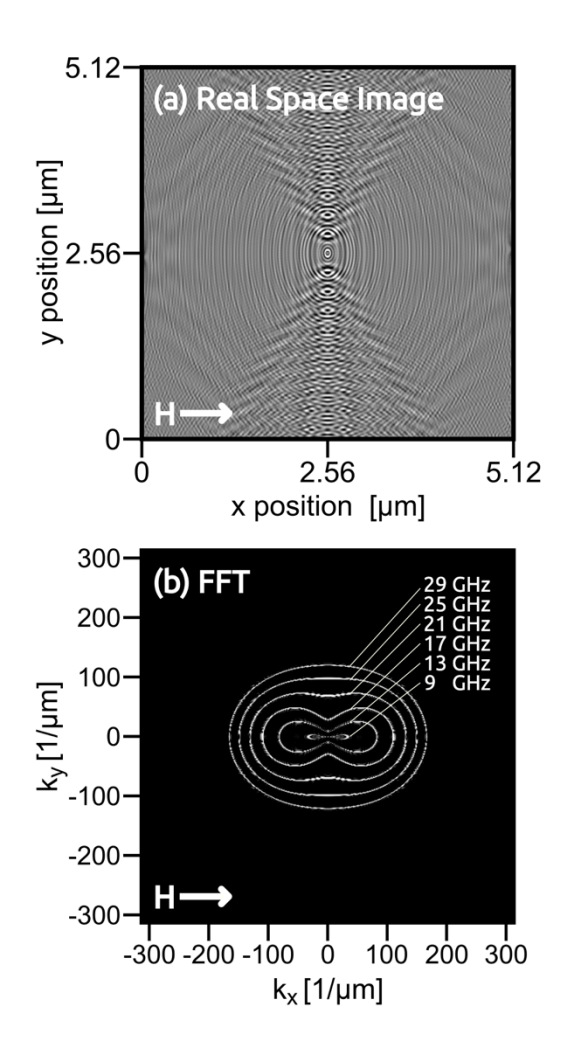


Figure 4: (a) Example of the spatial pattern of the transverse magnetization produced for a Permalloy film of thickness $t_{FM1}=30$ nm with H_{dyn} applied to a single central cell and $\mu_oH=0.1$ T along the x axis ($\phi=0$). Light regions indicate a positive value of m_z and dark regions have negative values. (b) A 2D spatial Fourier transform of the data from (a) produces isofrequency curves.

We allow the excitation to propagate until it nearly reaches the edges of the sample, about 2 ns. We then take the instantaneous values of one of the transverse components of the magnetization, illustrated in Fig. 4(a), typically the out-of-plane component m_z , and do a two-dimensional spatial Fourier transform. This produces a set of isofrequency curves in k space as

shown in Fig. 4(b). We note that the isofrequency curves calculated in this way agree with the results from analytic calculations done in Ref. [42] for dipole exchange modes.

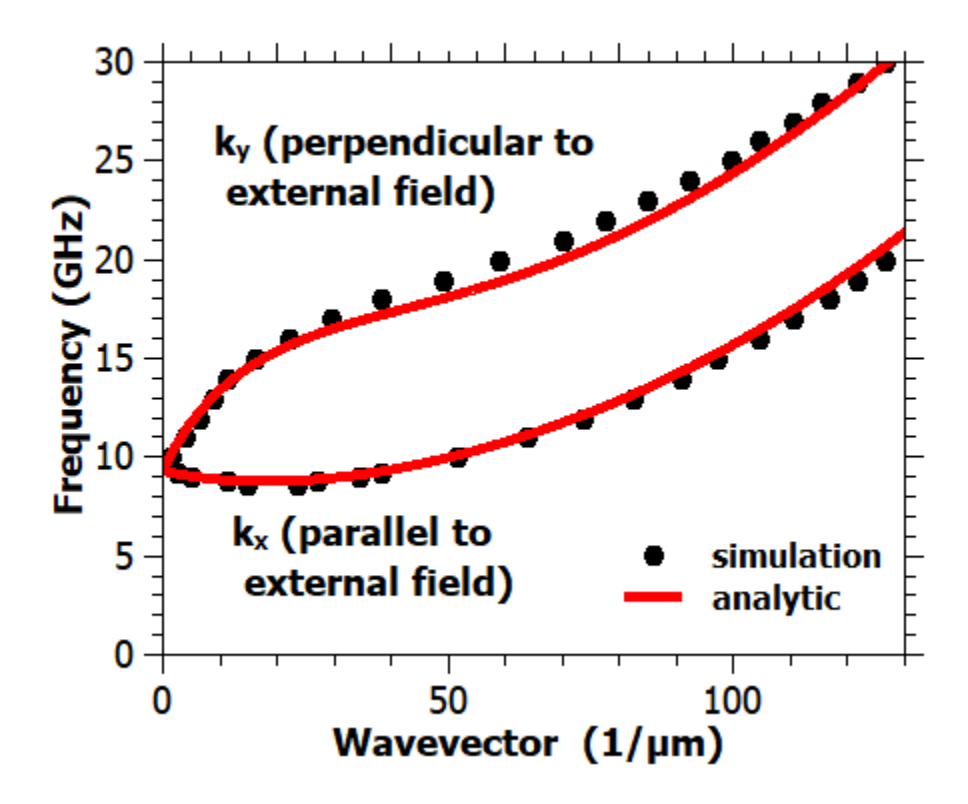


Figure 5: Dispersion relation obtained from several sets of isofrequency curves similar to those shown in Fig. 4. We generate dispersion relations for two propagation directions, parallel and perpendicular to the applied field. Analytic results, in red, for the same parameters are shown for comparison.

By this method, one can easily produce isofrequency curves (in 3D) in any direction. Also, if one wants an actual dispersion relation, one can drive the system at multiple frequencies (in a single run) and find the associated k values for each frequency. Then, taking the k values along a particular direction, one can obtain a dispersion curve for any particular direction as seen in Fig. 5. In this case we examine propagation both parallel and perpendicular to the applied field. We also provide the analytic results, calculated using the methods from Ref. [42]. The results are in very good agreement and would likely be better if one included more than 1 cell representing the thickness of the film in the micromagnetic calculations.

When implementing this method, it is important to consider if the strength of the driving field or the compilation of several driving fields could unintentionally push the system into the nonlinear regime. If the system is in the nonlinear regime, one will likely see the formation of second or higher harmonics and in the case where multiple driving frequencies are being explored simultaneously, one could see the formation of mixed frequencies^{43,44}. If there are several

different driving frequencies, the isofrequency curves of unintended nonlinear frequencies may be indistinguishable from their linear counterparts.

We note that, while this method also produces dispersion relations, it may not be as convenient as the method presented in the previous section. There are two reasons for this:

1) If there are many exciting frequencies and they are close together, the isofrequency curves may not be sufficiently resolved to cleanly associate a particular wavevector with a particular frequency. The resolution in *k*-space for the example above is given by

$$\Delta k = \frac{2\pi}{total\; distance} = \frac{2\pi}{(cell\; size)(number\; of\; cells)} = \frac{2\pi}{(5\; \text{nm})(1024)} = \; 1.23/\mu\text{m}$$

From the dispersion relation, this typically leads to a range of frequency values which is on the order of 0.5 GHz. This could be improved by using a larger structure.

2) In some cases, for example as seen in magnetostatic backward volume waves (along the x-direction), there are multiple k values for a single frequency. This can make it more difficult to write a program to associate k values with individual frequencies through a single set of isofrequency curves.

As a final comment on dispersion curves, the periodicity introduced by the choice of a cell size greater than the actual atomic spacing of material produces an effective first Brillouin zone, with edge value $k_{max} = \pi/(cell\ dimension)$ which is nonphysical. This results in the dispersion curve bending over at an inflection point near the center of this effective first Brillouin zone, artificially lowering the frequency values. This effect can be reduced by running the simulation with smaller cell sizes and thereby extending the size of the effective Brillouin zone. For the parameters explored in Fig. 5, a cell size of 10 nm gave good results up to about $100/\mu m$. When the cell size is reduced to 5 nm the region of accurate results extends to about $150/\mu m$.

In finite systems, it is important to address the impact of reflections on the results. One method to avoid the question of reflections is to simply not let the waves reach the boundaries of the system. We have found that reasonable isofrequency curves can be produced even if the excitation has not propagated very far away from the central point driven by the oscillating field. However, as one would expect, the resolution in k space is better if one allows the waves to propagate closer to the edge of the sample. Of course, the waves do not propagate equally quickly in all directions, so there is not a single time when the edge of the sample is reached. However, this does not significantly impact the quality of the isofrequency curves.

Isofrequency curves for finite size magnetic structures with dimensions on the order of hundreds of nm or smaller are different, however, from those obtained for larger objects. We illustrate this in Fig. 6, which compares some isofrequency curves obtained for a 30-nm thick Permalloy extended film and Permalloy square with a side length of 320 nm and the same thickness. As one would expect, in the small square the wavevectors are quantized, which leads to discrete

isofrequency points rather than the continuous curves that are found in an unconfined magnetic film. As a result, only a few wavevectors are excited at each driving frequency, but the discrete isofrequency points for the smaller square all lie almost directly on the isofrequency curve for the larger system as can be seen in Fig. 6(a). Which k values appear depends on the driving frequency and the dimensions of the magnetic structure. With substantial damping ($\alpha=0.05$), the eigenfrequencies are smeared out, and even for the small system, most of the isofrequency curve is present as seen in Fig. 6(b)

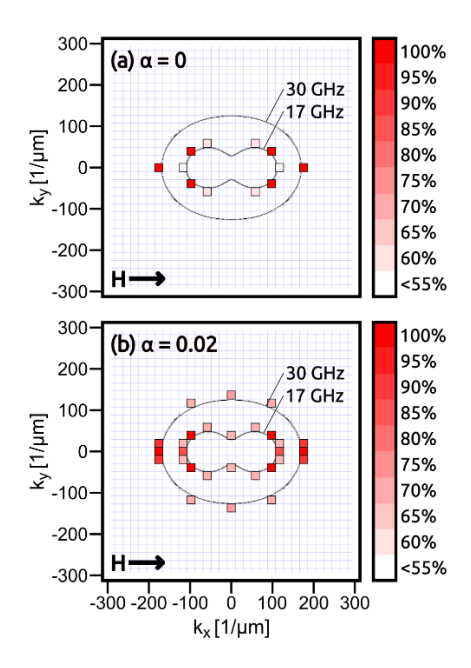


Figure 6: Isofrequency curves for a large structure (solid line) and small structure (squares). In (a) the damping is zero while in (b) the damping is large at $\alpha=0.02$. The parameters for the runs are as follows. For the large structure, the cell sizes are $5 \times 5 \times 30 \text{ nm}^3$; $1024 \times 1024 \times 1 \text{ cells}$; $\mu_o H=0.1 \text{ T}$. The small structure has the same parameters except the number of cells is $64 \times 64 \times 1$, which corresponds to a $320 \times 320 \text{ nm}^2$ square. The grid indicates the allowed k values for the small structure.

As a final example, we demonstrate the construction of isofrequency curves for a more complex situation where one has a ferromagnetic film with both interfacial DMI and perpendicular anisotropy. Such curves were used to demonstrate nonreciprocal power flow in DMI systems.³⁹

The parameters for this calculation were: cell size $10 \times 10 \times 1 \text{ nm}^3$, grid size $512 \times 512 \times 1$, applied field $\mu_o H = 0.8 \text{ T}$. The other parameters are the same as those in Ref. [39], i.e., out of plane anisotropy $K_u = 10^6 \text{ J/m}^3$, $A_{ex} = 15 \text{ pJ/m}$, $D = 1 \text{ mJ/m}^2$, $\alpha = 0.001$, $M_s = 10^6 \text{ A/m}$). Fig. 7(a) shows the spatial pattern created by a small source near the origin driven with an oscillating field of $\mu_o H_{dyn} = 0.002 \text{ T}$ at a frequency of 6 GHz. Fig. 7(b) is the spatial Fourier transform of the

entire spatial pattern. Despite the fact that the spatial pattern is strongly asymmetric, the resulting isofrequency curve is symmetric in *k*-space.

We can however get additional insight by taking the Fourier transform of the right (cyan box) and left (red box) sides separately. The result of this is shown in color-coded Fig. 7(c) where the cyan portion of the isofrequency curve comes from the right side of the original image, and the red portion from the left side. It is easy to see that the right side of the original image has waves with shorter wavelengths and thus provides information at the larger k vector values in Fig. 7(c). Similarly, the left side of the original image gives the portion of the isofrequency curve with smaller k values.

The final isofrequency curve is shown in Fig. 7(d), obtained by combining the appropriate portions of the curves seen in Fig. 7(c). It is not immediately clear which portions belong in the final isofrequency curve. We use the idea that the isofrequency curve and its slope should both be continuous. This guarantees that the power flow, which depends on the curvature of the isofrequency curve, is physical at all points.

The final isofrequency curve found here is equivalent to that in Ref. [39]. We mention, however, that the calculations of the isofrequency curves in Ref. [39] were done using the ultra-thin film approximation, and with a large in-plane magnetic field to saturate the structure, because analytical results for the general case are complicated. No such restriction occurs in generating isofrequency curves using micromagnetic data. One can treat thicker films, deal with antiferromagnetically coupled layers, and even deal with systems that are not saturated.

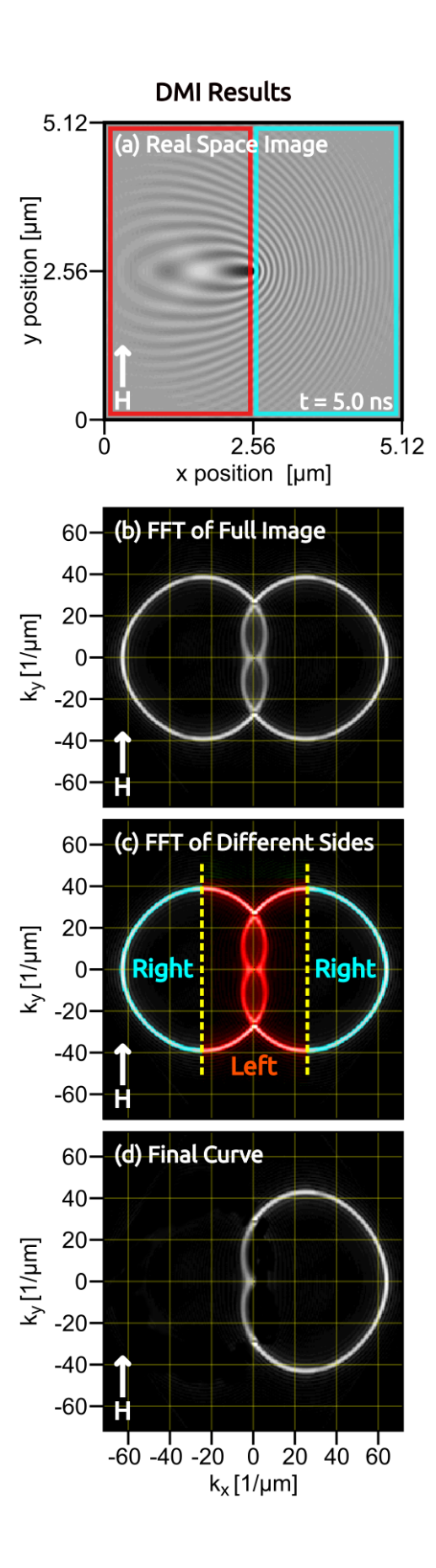


Figure 7: Spatial profile and calculated isofrequency curves for a Permalloy thin film of thickness 1 nm with interfacial DMI. The static field is $\mu_o H = 0.8 \text{ T}$ (a) shows the spatial pattern for m_z at t=2 ns. (b) isofrequency curve calculated from the Fourier transform of the entire spatial pattern. (c) color-coded portions of the isofrequency curves from the right (green) and left (red) sides of the spatial pattern. (d) final isofrequency curve as described in the text.

4) Summary

We have presented methods to calculate dispersion relations and isofrequency maps using micromagnetic simulations, and we show examples of how these methods can be used to study spin waves in thin film microstrips with arbitrary field angles, the effects of tilted antennas, and complex multilayer film stacks with DMI. These methods for obtaining dispersion relations and isofrequency curves are straightforward, flexible, and powerful, and provide important tools for understanding spin wave behavior in complex situations. Dispersion relations and isofrequency curves provide more complete insight into spin dynamics as compared to the more typically used micromagnetic simulation approach, which is to exactly replicate a particular experimental setup, and the presented methods provide a means to obtain these vital curves for magnetic thin film stacks and/or excitation geometries that go beyond the simple geometries that are analytically tractable. Since dynamic processes are of key importance to a wide range of magnetics problems, many of which involve complex setups, we expect that these methods will be useful for many topics of current interest including magnonics, spin torque nano-oscillators, quantitative measurements of DMI and critical parameters, the spin Seebeck effect, phonon/magnon and photon/magnon coupling that are important for quantum magnonics, and power flow in magnetic films.

We have dealt with issues relating to cell size throughout the paper and summarize the results here. The optimum choice of cell size depends on context. If computation time is not an issue, one can simply use a small cell size (3 nm on a side) and a large number of cells (4096 on a side). This a total side length of 12.3 μm and a wavevector resolution of 0.51/ μm . In a square film with only 1 cell thickness, this would involve over 16 million cells. With larger systems or systems with more than 1 cell in thickness the number increases substantially. In that case one might want to use larger cells, with the caveat that one wants to use cell sizes which are on the order of 1/10 of the shortest wavelength of interest. Thus, larger cells are allowed in the magnetostatic limit where the longer wavelengths are more important, and conversely, for spin waves in the exchange dominated region smaller cells are more appropriate. Clearly if one is dealing with excitations in domain walls or other magnetic textures, small cell sizes, on the order of a few nm, are a requirement. It is always a good idea to run simulations with different cell sizes to see if they agree; this can be particularly important for system with large anisotropies or short wavelengths where the magnetization direction can change rapidly as a function of position.

The impact of reflections has also been a continuous issue throughout this paper. We have used a number of methods to avoid reflections of spin waves at the boundaries. This included imposing regions of high damping near the edges of samples or simply only examining the

magnetic dynamics for times where the excitation has not yet reached the edges of the samples. Both methods work well, but in fact, reflections in many cases do not degrade the resulting dispersion relations or isofrequency curve results. For small systems, reflections are necessary in order to capture the quantization of the allowed modes.

Acknowledgements

We thank Carla Quispe Flores for helpful discussions of the dispersion relation approach. Work at CSU is supported by the National Science Foundation DMR #1709525 and the W. M. Keck Foundation.

References

- ¹ D.D. Stancil and A. Prabhakar, *Spin Waves: Theory and Applications*, 1st ed. (Springer, New York, 2009).
- ² A. Mahmoud, F. Ciubotaru, F. Vanderveken, A. V. Chumak, S. Hamdioui, C. Adelmann, and S. Cotofana, J. Appl. Phys. **128**, 161101 (2020).
- ³ A.A. Serga, A. V Chumak, and B. Hillebrands, J. Phys. D. Appl. Phys. **43**, 264002 (2010).
- ⁴ A. Khitun and K.L. Wang, Superlattices and Microstructures **38**, 184 (2005).
- ⁵ M.P. Kostylev, A.A. Serga, T. Schneider, B. Leven, and B. Hillebrands, Appl. Phys. Lett. **87**, 153501 (2005).
- ⁶ H.T. Nembach, J.M. Shaw, M. Weiler, E. Jué, and T.J. Silva, Nat. Phys. **11**, 825 (2015).
- ⁷ A.A. Stashkevich, M. Belmeguenai, Y. Roussigné, S.M. Cherif, M. Kostylev, M. Gabor, D. Lacour, C. Tiusan, and M. Hehn, Phys. Rev. B **91**, 214409 (2015).
- ⁸ K. Uchida, S. Takahashi, K. Harii, J. Ieda, W. Koshibae, K. Ando, S. Maekawa, and E. Saitoh, Nature **455**, 778 (2008).
- ⁹ M.J. Hurben and C.E. Patton, J. Appl. Phys. **83**, 4344 (1998).
- ¹⁰ B. Heinrich, J.F. Cochran, and R. Hasegawa, J. Appl. Phys. **57**, 3690 (1985).
- ¹¹ H.J.J. Liu, G.A. Riley, C.L. Ordóñez-Romero, B.A. Kalinikos, and K.S. Buchanan, Phys. Rev. B **99**, (2019).
- ¹² C.W. Sandweg, M.B. Jungfleisch, V.I. Vasyuchka, A.A. Serga, P. Clausen, H. Schultheiss, B. Hillebrands, A. Kreisel, and P. Kopietz, Review of Scientific Instruments **81**, 12 (2010).
- ¹³ G.T. Rado and R.J. Hicken, J. Appl. Phys. **63**, 3885 (1988).
- ¹⁴ B. Hillebrands, Phys. Rev. B **41**, (1990).
- ¹⁵ B.A. Kalinikos and A.N. Slavin, J. Phys. C Solid State Phys. **19**, 7013 (1986).
- ¹⁶ K.L. Livesey, D.C. Crew, and R.L. Stamps, Phys. Rev. B **73**, 184432 (2006).
- ¹⁷ M. Buchmeier, B.K. Kuanr, R.R. Gareev, D.E. Bürgler, and P. Grünberg, Phys. Rev. B **67**, 184404 (2003).
- ¹⁸ R.E. Camley, T.S. Rahman, and D.L. Mills, Phys. Rev. B **27**, 261 (1983).
- ¹⁹ P.A. Grunberg, Progress in Surface Science **18**, 1 (1985).

- ²⁰ J.F. Cochran and J.R. Dutcher, J. Appl. Phys. **63**, 3814 (1988).
- ²¹ V.E. Demidov, S.O. Demokritov, K. Rott, P. Krzysteczko, and G. Reiss, Phys. Rev. B 77, 4 (2008).
- ²² K.Y. Guslienko, S.O. Demokritov, B. Hillebrands, and A.N. Slavin, Phys. Rev. B **66**, 1 (2002).
- ²³ K.Y. Guslienko and A.N. Slavin, J. Magn. Magn. Mater. **323**, 2418 (2011).
- ²⁴ M.P. Kostylev, G. Gubbiotti, J.-G. Hu, G. Carlotti, T. Ono, and R.L. Stamps, Phys. Rev. B **76**, 054422 (2007).
- ²⁵ M.J. Donahue and D.G. Porter, *OOMMF User's Guide, Version 1.0* (Gaithersburg, MD, 1999).
- ²⁶ A. Vansteenkiste, J. Leliaert, M. Dvornik, M. Helsen, F. Garcia-Sanchez, and B. Van Waeyenberge, AIP Adv. **4**, 107133 (2014).
- ²⁷ V. Veerakumar and R.E. Camley, Phys. Rev. B **74**, 214401 (2006).
- ²⁸ B. Taylor, H.J. Maris, and C. Elbaum, Phys. Rev. Lett. **23**, 416 (1969).
- ²⁹ A.G. Every, Phys. Rev. B **34**, 2852 (1986).
- ³⁰ P. Taborek and D. Goodstein, Solid State Commun. **33**, 1191 (1980).
- ³¹ R.E. Camley and A.A. Maradudin, Phys. Rev. B **27**, 1959 (1983).
- ³² M. Kostylev, J. Appl. Phys. **115**, 233902 (2014).
- ³³ J.H. Moon, S.M. Seo, K.J. Lee, K.W. Kim, J. Ryu, H.W. Lee, R.D. McMichael, and M.D. Stiles, Phys. Rev. B **88**, 184404 (2013).
- ³⁴ G. Venkat, D. Kumar, M. Franchin, O. Dmytriiev, M. Mruczkiewicz, H. Fangohr, A. Barman, M. Krawczyk, and A. Prabhakar, IEEE Trans. Magn. **49**, 524 (2013).
- ³⁵ H.J. Liu, A. Guerrero, K.E. Nygren, M. Swyt, and K.S. Buchanan, Appl. Phys. Lett. **119**, 172403 (2021).
- ³⁶ X. Wang, A. Stuart, C.M. Quispe Flores, A.T. Clark, A. Fiagbenu, R. V. Chopdekar, P.N. Lapa, Z. Xiao, D. Keavney, R. Rosenberg, M. Vogel, J.E. Pearson, S.G.E. te Velthuis, A. Hoffmann, K.S. Buchanan, and X. Cheng, Submitted (2022).
- ³⁷ T. Sebastian, K. Schultheiss, B. Obry, B. Hillebrands, and H. Schultheiss, Frontiers in Physics **3**, 35 (2015).
- ³⁸ T. Schneider, A.A. Serga, A. V. Chumak, C.W. Sandweg, S. Trudel, S. Wolff, M.P. Kostylev, V.S. Tiberkevich, A.N. Slavin, and B. Hillebrands, Phys. Rev. Lett. **104**, 197203 (2010).
- ³⁹ J.-V. Kim, R.L. Stamps, and R.E. Camley, Phys. Rev. Lett. **117**, 197204 (2016).
- ⁴⁰ A. Papp and G. Csaba, IEEE Magnetics Letters **9**, 3706405 (2018).
- ⁴¹ R.A. Gallardo, P. Alvarado-Seguel, A. Kákay, J. Lindner, and P. Landeros, Phys. Rev. B **104**, 174417 (2021).
- ⁴² R.E. De Wames and T. Wolfram, J. Appl. Phys. **41**, 987 (1970).
- ⁴³ J. Marsh, V. Zagorodnii, Z. Celinski, and R.E. Camley, Appl. Phys. Lett. **100**, 102404 (2012).

⁴⁴ Y. Khivintsev, J. Marsh, V. Zagorodnii, I. Harward, J. Lovejoy, P. Krivosik, R.E. Camley, and Z. Celinski, Appl. Phys. Lett. **98**, 042505 (2011).